Nano Energy 133 (2025) 110439

Contents lists available at ScienceDirect

Nano Energy

journal homepage: www.elsevier.com/locate/nanoen

Full paper

Achieving stable lithium metal anode via constructing lithiophilicity gradient and regulating Li_3N-rich SEI

Xi Wang [a], Zhen Chen [a,*], Xilai Xue [b,c], Jian Wang [b,c,d], Yuxuan Wang [a], Dominic Bresser [b,c], Xin Liu [a,*], Minghua Chen [a,*], Stefano Passerini [b,c,e,**]

[a] Key Laboratory of Engineering Dielectric and Applications (Ministry of Education), School of Electrical and Electronic Engineering, Harbin University of Science and Technology, Harbin 150080, China
[b] Helmholtz Institute Ulm (HIU), Ulm 89081, Germany
[c] Karlsruhe Institute of Technology (KIT), Karlsruhe 76021, Germany
[d] Key Laboratory of Multifunctional Nanomaterials and Smart Systems & i-lab, Suzhou Institute of Nano-Tech and Nano-Bionics Chinese Academy of Sciences, Suzhou, Jiangsu 215123, China
[e] Austrian Institute of Technology (AIT) Transportation Technologies, Giefinggasse 4, Wien 1210, Austria

ARTICLE INFO

Keywords:
3D current collectors
Li metal anodes
"Bottom-up" Li deposition
Lithiophilicity gradient
Li_3N-rich SEI
Battery

ABSTRACT

Three-dimensional (3D) current collectors are studied for the application of Li metal anodes in high-energy battery systems. However, they still suffer from the preferential accumulation of Li on the outermost surface, resulting from an inadequate regulation of the Li^+ transport. Herein, we propose a deposition regulation strategy involving the creation of a 3D lithiophilicity gradient structure of MoN on Cu_3N nanowire-grown Cu foam (MCNCF) to induce a "bottom-up" Li deposition. During the initial Li deposition, the reaction between Li and Cu_3N leads to the formation of Li_3N while the lithiophilic MoN located at the bottom promotes the downward Li^+ migration, resulting in the generation of a Li_3N gradient. Such a "bottom-up" Li_3N distribution results in the formation of a stable and Li_3N-rich solid electrolyte interphase layer, facilitating the Li^+ transport and promoting a uniform Li nucleation. Computational simulations and experimental results corroborate the preferential deposition of Li on the bottom of the substrate, leading to a uniform Li nucleation and growth throughout the electrode. The MCNCF electrode offers a significantly improved reversibility of the Li deposition, achieving a lifespan of more than 1200 h at a current density of 1 mA cm^{-2} in symmetric Li||Li cells. Furthermore, full-cells incorporating MCNCF@Li as the negative electrode and $LiFePO_4$ cathodes exhibit outstanding electrochemical performance with a capacity retention of over 99.5 % after 250 cycles at 1 C, which significantly surpasses the performance achieved with CF@Li or CCF@Li electrodes. This innovative design strategy for 3D metallic current collectors, featuring a lithiophilicity gradient, provides new perspectives for the development of stable Li metal anodes and, as a result, for the advancement of Li-metal batteries.

1. Introduction

The global energy crisis and unprecedented demand for electrical energy necessitate the development of sustainable electrical energy storage technologies.[1] Among them, rechargeable batteries with high energy densities play a pivotal role. Lithium (Li) metal, characterized by a high theoretical specific capacity (3860 mAh g^{-1}) and very low redox potential (−3.04 V *vs.* standard hydrogen electrode), stands out as a prime candidate among various anode choices.[2,3] However, the widespread implementation of Li metal anodes (LMAs) encounters significant challenges, i.e., inhomogeneous Li deposition, substantial volumetric changes during plating/stripping processes, and the propensity to form a fragile solid electrolyte interphase (SEI).[4–6] These factors favor the emergence of Li dendrites and electrochemically inactive "dead Li", posing notable safety risks for Li-metal batteries (LMBs).[7,8] Furthermore, the loss of Li and electrolyte contributes to a reduced Coulombic efficiency (CE) and shortens the overall lifespan.

In recent years, great efforts have been dedicated to addressing these challenges. One approach is the utilization of three-dimensional (3D) hosts for LMAs, which helps to reduce the local current density and

* Corresponding authors.
** Corresponding author at: Helmholtz Institute Ulm (HIU), Ulm 89081, Germany.
E-mail addresses: chen.zhen@hrbust.edu.cn (Z. Chen), liu.xin@hrbust.edu.cn (X. Liu), mhchen@hrbust.edu.cn (M. Chen), stefano.passerini@kit.edu (S. Passerini).

https://doi.org/10.1016/j.nanoen.2024.110439
Received 8 July 2024; Received in revised form 7 October 2024; Accepted 31 October 2024
Available online 3 November 2024

accommodate the volume changes occurring during cycling. Among the available options, Cu foam (CF) is commonly chosen due to its inertness versus Li as well as its porous structure, which can accommodate a large amount of lithium and mitigate the overall volume expansion.[9] However, the inherent poor lithiophilicity of Cu presents a high barrier for Li nucleation and leads to an unstable SEI. To overcome these limitations, the integration of materials such as Zn,[10] ZnO,[11] Co_3O_4,[12] Mo_2C,[13] and Ag,[14] which exhibit pronounced lithiophilicity, is deemed essential for promoting a homogeneous Li nucleation. Unfortunately, the incorporation of these materials often leads to reduced conductivity or increased cost of the current collector. Thus, a surface modification strategy that balances lithiophilicity with conductivity is urgently needed.

Li_3N has emerged as a promising material in this context, effectively restraining Li dendrite growth thanks to its high ionic conductivity (10^{-3}-10^{-4} S cm^{-1}), low electronic conductivity (< 10^{-12} S cm^{-1}), favoring Li deposition at the interface between Cu metal and Li_3N, excellent thermodynamic stability and high Young's modulus.[15,16] For example, Tang et al.[17] fabricated a current collector with Cu_3N nanowires on a Cu foil (Cu_3N NWs/Cu) through a simple chemical method. During the initial Li plating process, the Cu_3N reacted with Li to form a Li_3N-rich SEI, which demonstrated high ionic conductivity and mechanical strength. Cao et al.[18] developed a 3D host with a gradient Li_3N *in situ* formed on a carbon-based framework using a molten lithium method (denoted as CC/Li/Li_3N). Density functional theory (DFT) calculations revealed that Li_3N can effectively promote the transport of Li^+ due to its low energy barrier for the Li^+ diffusion. Hence, the combination of a Li_3N artificial interface and a 3D host represents a promising strategy for stabilizing the interface, guiding the homogeneous Li deposition, and relieving the volume changes of LMAs.

However, the uniform lithiophilicity and conductivity of a 3D host often leads to preferred Li deposition on the top surface, attributed to shorter Li^+ diffusion pathways and an unregulated Li^+ flux.[19] To address this, we introduce a novel, straightforward deposition strategy to achieve a "bottom-up" growth of the Li anode, realizing a 3D lithiophilicity gradient structure of MoN on a Cu_3N nanowire-grown Cu foam (MCNCF). The introduction of nanowire structures on the CF surface does not only increase the specific surface area of the current

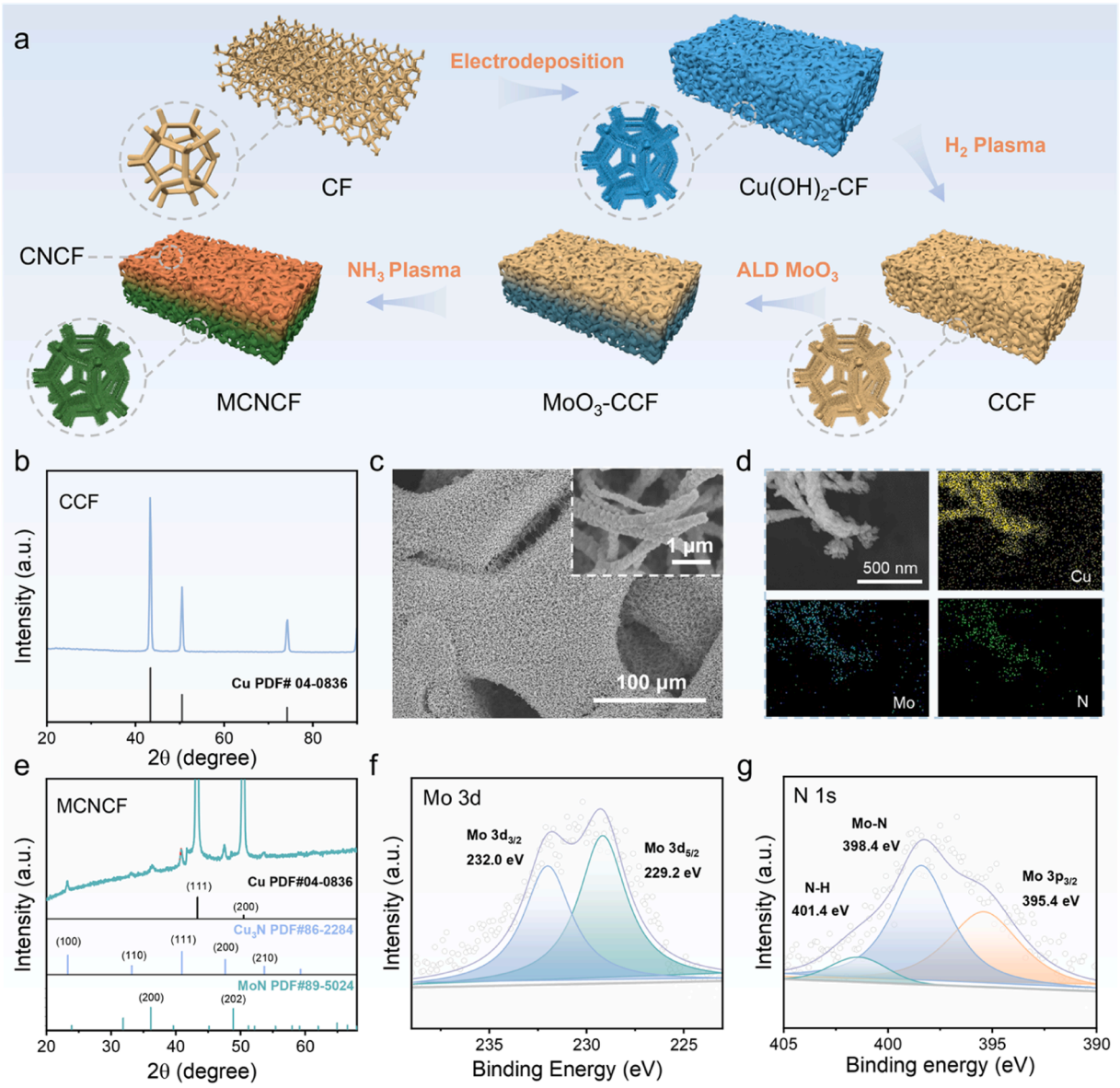

Fig. 1. (a) Schematic illustration of the preparation process of MCNCF. (b) XRD pattern of CCF. (c) SEM images of MCNCF and (d) corresponding EDS mapping results. (e) XRD pattern of MCNCF. XP spectra of the (f) Mo 3d and (g) N 1 s of MCNCF.

collector, reducing the current density on its surface, but moreover accommodates the volumetric changes that occur during Li deposition/stripping processes. Moreover, during the initial Li deposition, a reaction occurs between Cu_3N and Li, leading to the formation of Li_3N. The bottom lithiophilic MoN favors Li^+ migration downwards, generating more Li_3N and establishing a "bottom-up" Li_3N gradient within the electrode. As a result, a stable SEI layer rich in Li_3N is formed, which enhances the Li^+ transport and provides abundant nucleation sites for a uniform lithium deposition. The distinctive lithiophilicity gradient within the MCNCF structure underpins its exceptional electrochemical performance, enabling consistent and reversible Li deposition/stripping. Furthermore, when integrated into a full-cell with $LiNi_{0.8}Co_{0.1}Mn_{0.1}O_2$ (NCM811) cathodes, the MCNCF anode demonstrates superior rate capability and exhibits long-term stable cycling performance. These findings highlight the potential of utilizing the MCNCF host as a candidate anode material for application in LMBs.

2. Result and discussion

2.1. Preparation and characterization of MCNCF

Fig. 1**a** illustrates the schematic illustration of the synthesis route of MCNCF. Concurrently, Fig. S1 captures the color change of the various samples (i.e., CF, $Cu(OH)_2$-CF, CCF and MCNCF) formed throughout the synthesis process. Initially, $Cu(OH)_2$ nanowires were electrodeposited onto CF via a rapid electrochemical deposition (denoted as $Cu(OH)_2$-CF). These nanowires then underwent thermal reduction using H_2 plasma treatment, leading to the formation of Cu nanowires (CCF). Subsequently, a thin and uniform MoO_3 layer was applied to the bottom of the CCF framework using atomic layer deposition (ALD). Mild NH_3 plasma treatment was then employed for low-temperature nitridation, converting CCF into Cu_3N-CF (CNCF) and forming a lithiophilic MoN layer at the bottom, thus, finalizing the MCNCF structure. To track the structural and morphological evolutions throughout the synthesis process, X-ray diffraction (XRD), scanning electron microscopy (SEM) and transmission electron microscopy (TEM) were performed. Pristine CF displays a 3D interconnected Cu framework with a porous mesh structure, displaying a smooth and impurity-free surface (Fig. S2a). As evident from Fig. S2b, the $Cu(OH)_2$ nanowires grew uniformly on the CF skeleton. The inset high-magnification SEM image illustrates that the nanowires exhibit a smooth surface and diameter ranging between 50 nm and 100 nm. The formation of $Cu(OH)_2$ is verified by XRD (Fig. S3, PDF#35–0505). The absence of the characteristic reflections for $Cu(OH)_2$ in the XRD pattern of CCF (Fig. 1**b)** indicates the complete conversion of $Cu(OH)_2$ to metallic Cu after the H_2-based post-reduction treatment. Meanwhile, the integrity of the nanowire morphology is well-maintained, as depicted in Fig. S2c.

Upon deposition of the MoN layer, the color of MCNCF changes from brown (CCF) to black (Fig. S1c**, d**). SEM images of MCNCF are presented in Fig. 1**c**, and energy dispersive X-ray spectroscopy (EDS) mapping confirms the uniform elemental distribution of the MoN layer on the nanowires (Fig. 1**d**). Moreover, the XRD results shown in Fig. 1**e** confirm the existence of Cu_3N (PDF#86–2284) and MoN (PDF#86–2284) in MCNCF, while only Cu_3N is present in CNCF (Fig. S4). Cross-sectional EDS elemental mapping results (Fig. S5b **and d**), corresponding to the SEM image (Fig. S5a), confirm that the nitridation degree increases from the top to the bottom of the MCNCF framework, verifying a gradient distribution of MoN (Fig. S5). The TEM images show a homogeneous coating layer on the surface of MCNCF, which thickness ranges from 32 to 37 nm (Fig. S6). Further high-resolution TEM (HRTEM) analysis (Fig. S7) identifies distinctive lattice fringes corresponding to the MoN (002), MoN(200), and MoN(202) planes in the coating layer, as well as the Cu_3N(111) and Cu_3N(211) planes in the inner layer of MCNCF. X-ray photoelectron spectroscopy (XPS) analysis of MCNCF reveals distinct peaks at 232.1 and 228.9 eV in the Mo 3d spectrum, corresponding to Mo $3d_{3/2}$ and Mo $3d_{5/2}$ of the Mo-N bonds, respectively (Fig. 1**f**). Additionally, the N 1 s XP spectrum displays deconvoluted peaks at 401.4 and 398.4 eV, corresponding to the N-H, Mo-N bonds, respectively (Fig. 1**g**). Notably, the Mo $3p_{3/2}$ contribution partially overlaps with the N 1 s peak, leading to an observable peak located at 394.9 eV in the N 1 s XP spectrum.[20,21] Furthermore, the absence of peaks in the Cu 2p spectrum further confirms that the coating layer is predominantly composed of MoN (Fig. S8). In summary, the Cu nanowires are successfully nitridated to Cu_3N, and the bottom MoO_3 is transformed into MoN, thus, forming a structure with a gradient of the nitrogen content, decreasing from the bottom to the top.

2.2. Investigation of the chemical adsorption/diffusion regulation properties

To investigate the electrical properties, the electrical conductivity of CF, CNCF, and MCNCF was measured using a four-point probe (Fig. S9). The results indicate that CF has the highest conductivity (3.33×10^{-4} S cm^{-1}), while the conductivity of MCNCF (2.00×10^{-4} S cm^{-1}) is slightly higher than that of CNCF (1.67×10^{-4} S cm^{-1}), suggesting a conductivity gradient within MCNCF that facilitates the migration of Li^+ towards the bottom. The assessment of the lithiophilic nature of the current collector can be quantified by measuring the nucleation overpotential, which is the difference between the lowest potential reached during the initial phase of electrodeposition and that of the plateau.[22] The comparative analysis illustrated in Fig. 2**a** reveals that MCNCF exhibits a significantly reduced Li nucleation overpotential of *ca.* 8.5 mV compared to the values recorded for CCF (43.6 mV) and CF (85.6 mV). This disparity highlights the superior lithiophilicity of MCNCF compared to CCF and CF.

To elucidate the underlying mechanism for the enhanced lithiophilicity of MCNCF, a comprehensive set of *in situ* and *ex situ* analyses and computational studies were conducted. It is known that lithiophilicity is closely associated with the intrinsic properties of materials. Therefore, prior to the lithiophilicity analysis, a clear picture of the involved materials is vital. In this regard, *operando* XRD was first performed to investigate the structural evolution of MCNCF upon lithiation and delithiation. The characteristic reflection of MoN, specifically the (200) plane, vanishes upon discharge MCNCF to 1.25 V. Similarly, the characteristic reflections of Cu_3N, including the (110), (111), and (200) planes, disappear when MCNCF is discharged to 0.5 V (Fig. 2**b**). Hereafter, no obvious reflections are observed even after the charge process, suggesting that the reaction products may be amorphous and that the structural changes experienced by MoN and Cu_3N during discharge are irreversible. From Fig. S10, the Mo 3d XP spectrum recorded after fully discharging MCNCF to 0.01 V demonstrates the formation of elemental Mo.[23] Meanwhile, XPS depth profiling with Ar^+ etching for varying durations was conducted to probe the SEI composition of CF and MCNCF-based electrodes. Notably, the Li_3N observed in the CF electrode diminishes after 100 s of Ar^+ etching (Fig. 2**c**), whereas that in the MCNCF electrode slightly increases upon etching (Fig. 2**d**), suggesting that the nitrogen supply from the MoN layer facilitates the formation of Li_3N.

Furthermore, the compositional analysis of the SEI reveals that the outermost layer predominantly consists of Li carbonate resulting from the electrochemical reduction of the electrolyte, which progressively decreases with an increasing sputtering time. Li carbonate is identified through the characteristic peaks at 289.8 eV in the C 1 s spectra (corresponding to C═O bonds) and at 55.1 eV in the Li 1 s spectra (indicative of Li_2CO_3). The deconvolution of the F 1 s XP spectra reveals two peaks located at 688.5 and 684.9 eV, corresponding to C-F and LiF, respectively. These peaks are indicative of decomposition products of LiTFSI, with a higher proportion of C—F observed in the CF-based electrode (Fig. S11). Additionally, the O 1 s XP spectra reveal two peaks at 532 and 531.2 eV, attributed to S—O and C—O/C═O species. The XPS results for the C 1 s, F 1 s, O 1 s, Li 1 s, and N 1 s peaks further suggest that organic constituents formed through the reductive

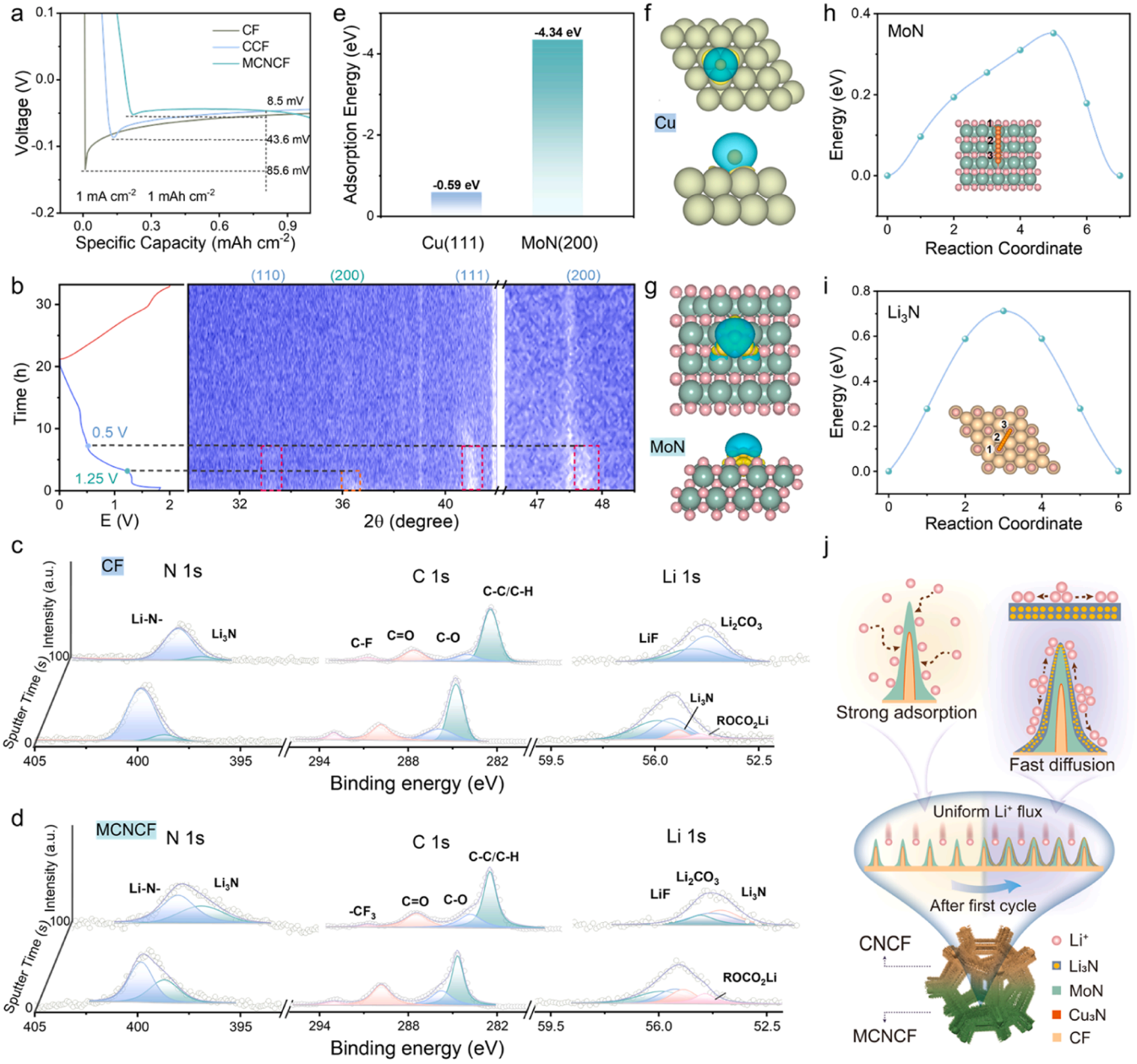

Fig. 2. (a) Deposition curves of Li on different electrodes. (b) *Operando* XRD results for the MCNCF electrode during the discharge-charge process. Depth profiles of the N 1 s, C 1 s, and Li 1 s XP spectra of (c) CF and (d) MCNCF electrodes after being discharged to 0.01 V. (e) Adsorption energy of Li on the Cu(111) and MoN(200) surface. Calculated electron density difference before and after the adsorption of Li on the (f) Cu(111) and (g) MoN(200) surfaces. Cyan and yellow isosurfaces (0.001 a.u.) represent an electron accumulation and depletion, respectively. Migration pathway and the corresponding Li diffusion barrier profile for the (h) Li_3N (001) and (i) MoN(200) surfaces. (j) Scheme highlighting the working mechanism of MCNCF upon Li deposition.

decomposition of the solvents and salt, including C—C/C—H, C—O, C═O, C—F, etc., and primarily constitute the upper layer of the SEI. XPS depth profiling discloses a decreased content of these organic components with a concomitant increase in inorganic constituents such as S—O, LiF, and Li_3N. These findings indicate that the lithiation of MCNCF results in the formation of a uniform Li_3N-rich SEI.

To evaluate the lithium affinity of both Cu and the MoN coating, density functional theory (DFT) calculations were conducted (Table S1). Fig. 2**e** presents compelling evidence that MoN(200) exhibits a significantly larger adsorption energy of −4.34 eV for lithium compared to Cu (111) with an adsorption energy of −0.59 eV. The designed structure facilitates enhanced Li deposition on the MoN surface at the bottom. Charge transfer analyses depicted in Figs. 2**f** and 2**g** reveal a more substantial charge transfer when a lithium atom is adsorped on the MoN surface in comparison to pure copper. This observation unequivocally confirms the superior lithium affinity of MoN *vs.* Cu.

The XPS results in Fig. S10 indicate the formation of Li_3N during the progression of battery cycling, resulting from the reaction between deposited lithium and MoN. To investigate the mobility of lithium in the generated Li_3N and MoN, which is crucial for understanding charge-discharge rates in rechargeable batteries, the climbing image nudged elastic band (CI-NEB) method was employed, and the corresponding migration pathways are depicted in Figs. 2**h and** 2**i**. Initially, intermediate images were linearly interpolated between the most stable sites. For the MoN(200) surface, the CI-NEB calculation reveals that the Li atom would migrate from the Mo top site to the nearest Mo top site with a rather small kinetic barrier (0.35 eV). In addition, the migration trajectory also implies that the saddle point locates at the Mo-N bridge site.

Besides, Li_3N exhibits rapid Li diffusivity with an energy barrier of 0.71 eV. These findings validate that MoN does not only promote the Li deposition at the bottom of the current collector, but also enables fast Li migration.

The lithiophilicity gradient design of the MCNCF framework, as depicted in Fig. 2**j**, offers the following advantages: (i) The nanowire structure on the CF skeleton increases the specific surface area of the current collector, reducing the local current density, and accommodates the volumetric changes during the Li plating and stripping processes. (ii) The constructed lithiophilicity gradient structure guides Li^+ towards the bottom of the electrodes. (iii) The reaction of Cu_3N and MoN with Li^+ yields a gradient distribution of the Li_3N-rich SEI. (iv) The Li_3N-rich SEI enhances rapid Li^+ transport and provides nucleation sites, promoting a uniform Li deposition. Consequently, it is theoretically predicted that the MCNCF electrode, leveraging strong adsorption and fast diffusion properties, is an effective approach to suppress dendrite formation and stabilize the LMAs.

2.3. Validation of the "bottom-up" Li deposition behavior of MCNCF

To evaluate the effectiveness of the MoN layer for the lithium nucleation and deposition, the electrochemical behavior of Li plating was examined via galvanostatically electrodepositing Li on CF, CCF and MCNCF current collectors at a current density of 0.25 mA cm^{-2}. The surface morphology analyses of various frameworks after Li plating reveal distinct morphologies. In the initial stage of electroplating on a CF electrode, an uneven nucleation is apparent from the presence of micro-Li particles and an exposed CF framework, which can be attributed to the high Li nucleation overpotential (Fig. 3**a_1, a_2,** and Fig. S12a). These particles subsequently act as prior nucleation centers, promoting the formation of elongated Li dendrites (Fig. 3**a_3**). As the Li plating capacity increases to 5 mAh cm^{-2}, many disordered Li dendrites (about 10 μm in diameter) spread throughout the CF pores (Fig. 3**a_4** and Fig. S12d), indicating that CF fails to enable a uniform Li nucleation and suppress dendrite growth[24] even in the case of a rather limited Li deposition. The CCF electrode, on the other hand, allows for a more homogeneous Li deposition through its porous structure at plating capacities of 0.01 and 0.5 mAh cm^{-2}, yet dendrite formation persists (Fig. 3**b_1, b_2** and Fig. S12b). The presence of Cu nanowires elevates the surface area and evenly distributes the charge. However, Li plating with capacities higher than 2 mAh cm^{-2} results in rapid dendrite growth (Fig. 3**b_3, b_4** and Fig. S12e). In stark contrast, the Li plating behavior of MCNCF outperforms the other two counterparts, confirming that the lithiophilicity gradient design enables both strong Li adsorption and fast Li diffusion. At low Li plating capacities (0.01 and 0.5 mAh cm^{-2}), compact Li nuclei form, promoted by the formation of a stable Li_3N-rich SEI (Fig. 3**c_1, c_2** and Fig. S12c). Further Li plating up to 2.0 mAh cm^{-2} results in MCNCF being uniformly enveloped by dense Li (Fig. 3**c_3**). Even after depositing 5 mAh cm^{-2} of Li, the top skeleton of MCNCF is still clearly visible and negligible Li dendrites are generated (Fig. 3**c_4** and Fig. S12f).

To gain real-time insights into the Li deposition behavior, *operando* techniques were employed. First, a home-designed cell (Fig. S13) was employed to observe the electrode evolution over prolonged deposition time. The rapid formation of pronounced dendritic structures on CF is observed within the first hour (Fig. S13a, Movie S1). Afterwards, the growth of dendrites becomes increasingly fast and erratic. From Fig. S13b and Movie S2, comparable dendritic lithium deposition is also noted on CCF after 1 h of Li plating. In contrast, MCNCF exhibits a smooth and dense morphology with very minor dendritic Li deposition after plating for 3 h (Fig. S13c and Movie S3).

Shifting our observation from the macro-scale to the micro-scale, an *in situ* optical microscope was used to capture the Li plating behavior on CF, CCF, and MCNCF electrodes. The Li||CF asymmetric cell shows severe dendrite growth after 0.5 h of Li plating, which rapidly grows and eventually leads to short circuiting and cell failure after 1 h (Fig. S14). The entire measurement for the CCF- and MCNCF-based cells lasts for 3 h at a current density of 2 mA cm^{-2}. In the former cell, small Li dendrites start to grow on the electrode surface after 1 h (Fig. 3**d_2**), implying a typical "top-deposition" behavior. After plating for 3 h, the Li dendrites severely overflow from the CCF electrode side (Fig. 3**d_3**). In a striking contrast, MCNCF exhibits a completely different Li plating behavior. Evident from Fig. 3**e_2**, the deposited Li is dispersed throughout the framework, and it can be clearly observed that more Li is deposited in the bottom region. Even after 3 h of Li plating, MCNCF still does not display obvious dendritic Li. Additionally, the Li deposition behavior on the pure CF electrode is similar to that on the CCF electrode, exhibiting apparent "top deposition" behavior within 3 h of Li deposition (Fig. S15). These results confirm that the construction of a lithiophilicity gradient within the MCNCF host structure promotes a stable electrode morphology, which can be ascribed to the protective effect of the gradient Li_3N. This configuration enhances Li deposition at the bottom of the 3D host and inhibits Li dendrite formation, leading to a preferential "bottom-up" Li deposition process.

Computational simulations of the Li deposition behavior were conducted using the COMSOL Multiphysics software. For the CCF framework with uniform conductivity and lithiophobicity, the incoming Li^+ ions preferentially accumulate on the top surface, resulting in dendritic growth through consecutive Li plating and stripping (Fig. 3**f**). However, the Li^+ flux distribution in the case of the MCNCF electrode shows a gradient over a large range, while maintaining a uniform distribution over a smaller range consistently throughout the entire domain (Fig. 3**g**). The COMSOL simulation reveals that the MCNCF electrode significantly modulates the distribution of the Li^+ flux, thereby optimizing the conditions for a homogeneous Li deposition. These results highlight the superiority of the 3D lithiophilicity gradient design of the MCNCF structure compared to the CF and CCF electrodes. It is evident that the gradient Li_3N is instrumental in enhancing the Li^+ transport, leading to the formation of a uniform and rapid Li^+ flux, which is critical for improving the anode (and battery) performance.

2.4. The impact of the electrode design on the electrochemical performance

Wetting tests with molten Li can verify the lithiophilicity of different electrode structures. Upon exposure to molten Li, rapid and thorough wetting is observed with the MCNCF discs (Fig. 4**a**). Comparative studies of the Li plating/stripping reversibility were performed by evaluating the CE among various current collectors in half-cell setups. As shown in Fig. 4**b**, under the 1 mAh cm^{-2} and 1 mA cm^{-2} regime, the MCNCF sustains an average CE of 98.0 % over 240 cycles, whereas the CCF and CF electrodes demonstrate inferior cycle life of *ca.* 140 (96.6 %) and 90 (91.9 %) cycles, respectively. The voltage profiles of MCNCF for different cycle numbers demonstrate an overlapping behavior **(**Fig. 4**c)**, indicating an excellent reversibility of Li plating and stripping. Increasing the current density to 3 mA cm^{-2}, the MCNCF maintains a high average CE value of 98.1 % over 110 cycles (Fig. 4**d)**. In contrast, both CCF and CF show a pronounced decline in average CE with only 95.9 % over 60 cycles and 93.3 % over 50 cycles, respectively, which should be due to the continuous formation of Li dendrites and consumption of the electrolyte. Additional tests were conducted at a capacity of 1 mAh cm^{-2} and current densities of 0.5 mA cm^{-2} and 2 mA cm^{-2}, where MCNCF always demonstrates pronounced advantages over CCF and CF (Fig. S16). The stability in CE and cycling performance of MCNCF underscores its superiority in promoting homogenous Li deposition and its enhanced reversibility during cycling – also in comparison to conventional collectors, as summarized in Table S2.

Electrochemical impedance spectroscopy (EIS) reveals that the interfacial resistance is lower for MCNCF than for CCF and CF in the 1st, 10th, and 50th cycle, as shown in Fig. 4**e** and Fig. S17. This denotes an improved surface compatibility with Li, uniform Li deposition, and accelerated Li plating/stripping kinetics – trends that align with the

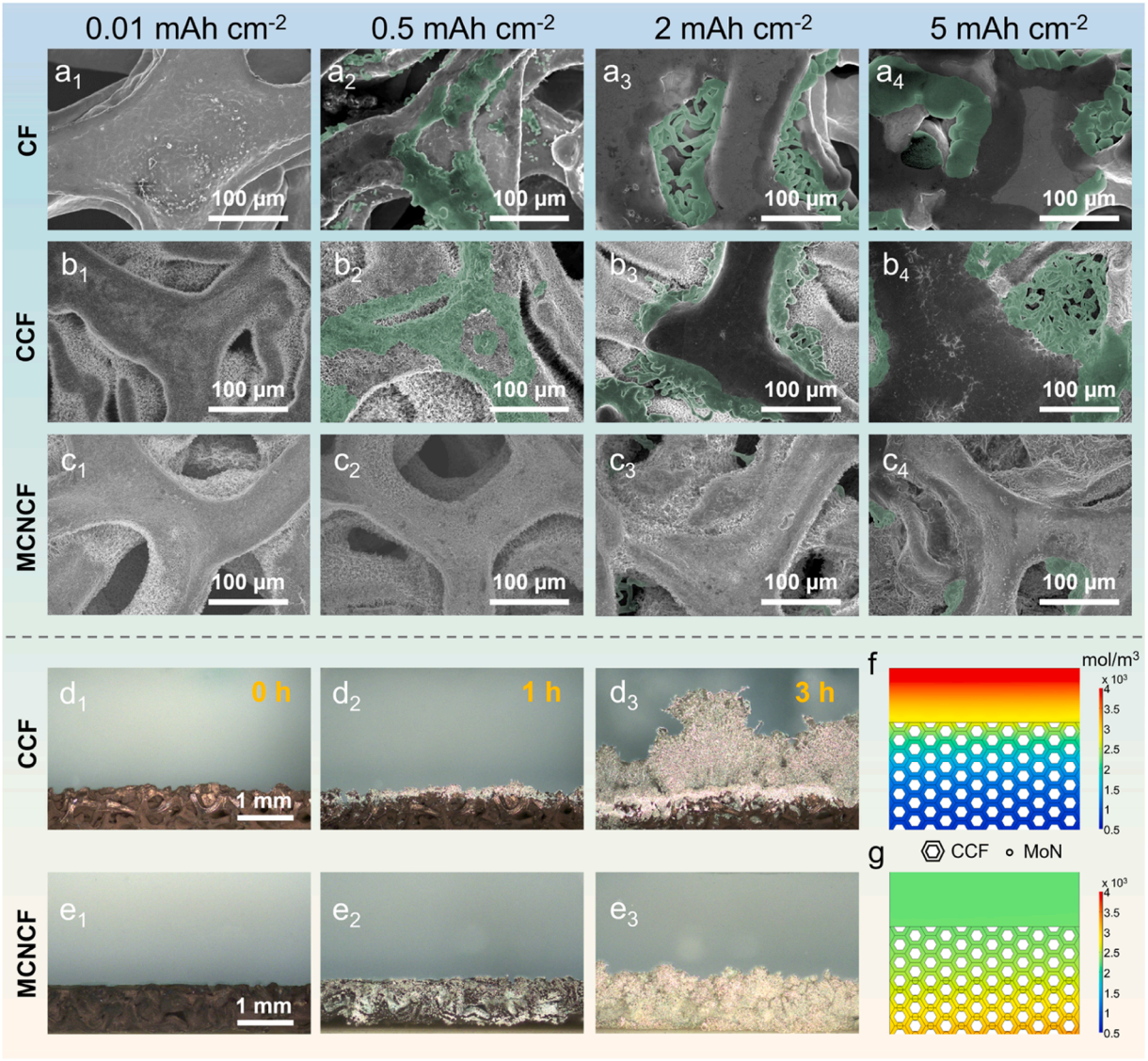

Fig. 3. Surface morphology evolution of (a) CF, (b) CCF, and (c) MCNCF electrodes with different Li deposition capacities (Li dendrites are clearly highlighted in light green color). The examination of the Li deposition behavior via *in situ* optical microscope of (d) CCF- and (e) MCNCF-based electrodes at a current density of 2 mA cm^{-2}. COMSOL simulations of the Li^+ flux distribution in the (f) CCF and (g) MCNCF frameworks.

observed reduction of the voltage hysteresis. However, a decrease in interfacial resistance is observed across all samples by the 50th cycle, potentially due to electrode surface roughening which reduces the charge transfer resistance by increasing the active area.

Symmetric Li||Li cells were further assembled to analyze the Li plating/stripping behavior. The symmetric cells containing the MCNCF@Li electrodes present a very constant overpotential during cycling, with negligible variation observed beyond 1200 h of operation at 1 mA cm^{-2} and 1 mAh cm^{-2} per cycle (Fig. 4**f**). This can be attributed to the excellent Li^+ ion conductivity of the Li_3N-rich SEI film, facilitating rapid Li^+ migration and diffusion. In stark contrast, symmetric cells employing CCF@Li and CF@Li electrodes show a significant increase in overpotential after 300 and 350 h, respectively. In addition, the symmetric MCNCF@Li cells exhibit a remarkably low voltage hysteresis of approximately 16 mV, outperforming those of the CCF@Li (22 mV) and CF@Li (20 mV) cells (Fig. S18). Upon elevating the current density to 2 mA cm^{-2}, the symmetric MCNCF@Li cells sustain a prolonged overpotential stability for 470 h with a hysteresis of 20 mV. In comparison, the CCF@Li and CF@Li cells can only maintain such stability for 250 and 150 h with a hysteresis of 40 and 38 mV, respectively (Fig. S19a). A further increase of the current density to 3 mA cm^{-2} reveals that the symmetric MCNCF@Li cells sustain an exceptionally flat voltage profile for 400 h and exhibit a very low voltage hysteresis of 23 mV (Fig. S19b). Differently, the symmetric CCF@Li and CF@Li cells show a progressive rise in overpotential, reaching 48 and 71 mV after 90 and 25 h, respectively. A subsequent assessment of the overpotential when applying an increased areal specific capacity of 3 mAh cm^{-2} (Fig. S19c) demonstrates that the CCF@Li and CF@Li electrodes could be cycled for only 700 and 500 h, respectively. In contrast, the MCNCF@Li electrodes provide a stable cycling performance for more than 900 h without significant voltage fluctuations.

Fig. 4**g** presents the evaluation of the rate capability of these electrodes by applying varying current densities of 0.5, 1, 2, and 5 mA cm^{-2}, with a fixed capacity of 1 mAh cm^{-2}. The resulting overpotential values for MCNCF@Li (13, 17, 28, 52 mV) are substantially lower and more consistent than those observed for CCF@Li (34, 40, 51, 81 mV) and CF@Li (41, 49, 64, 110 mV; Fig. 4**h**). These findings underscore the synergistic contribution of the multiporous architecture, which facilitates a reduction in effective current density, and the lithiophilicity gradient structure, both of which collectively modulating the Li

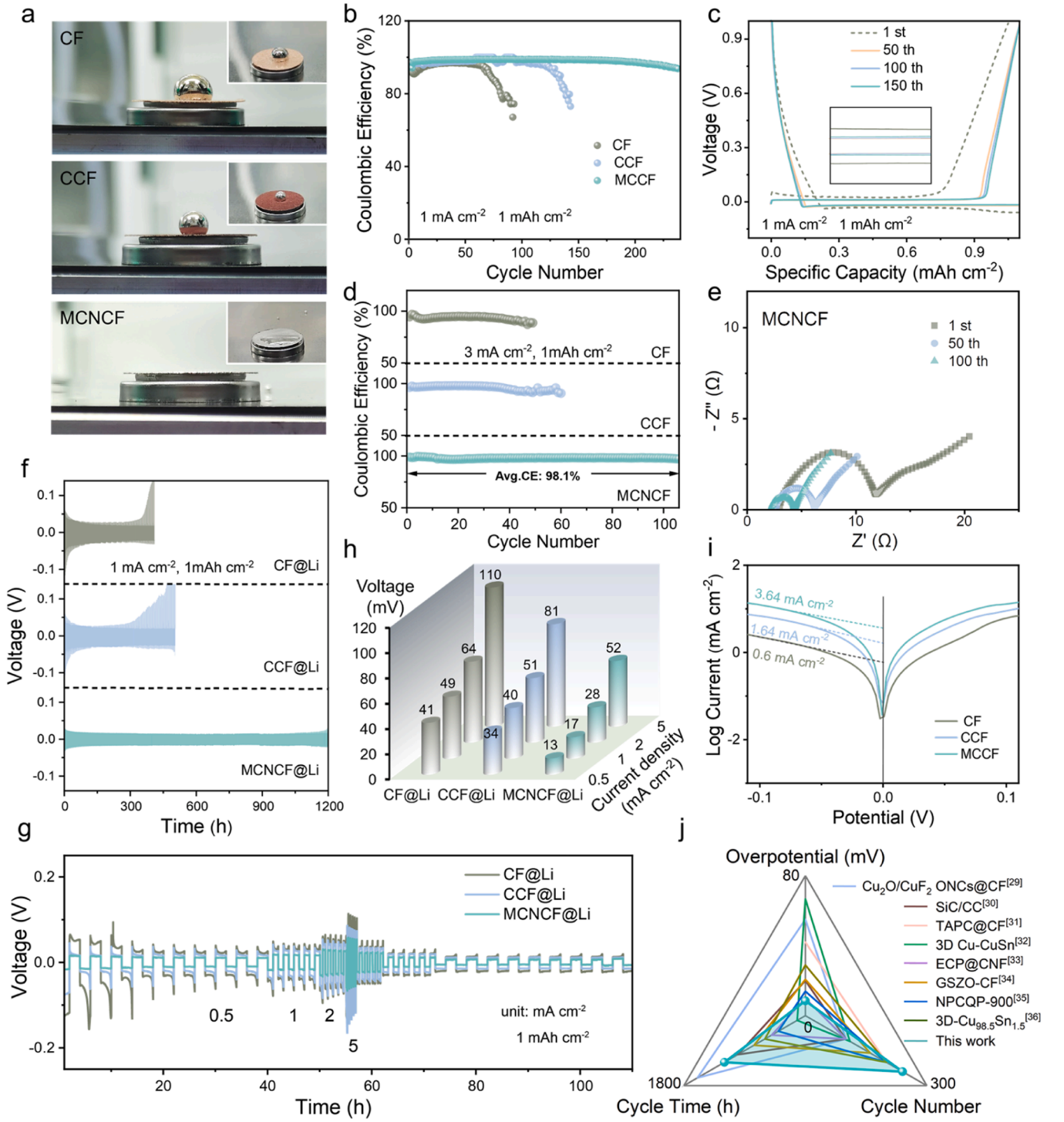

Fig. 4. (a) Lithiophilicity tests for CF, CCF and MCNCF. (b) The CE of CF, CCF and MCNCF electrodes upon Li plating/stripping at a current density of 1.0 mA cm^{-2}. (c) Selected voltage profiles and partially enlarged details of MCNCF. (d) The CE of CF, CCF and MCNCF electrodes upon Li plating/stripping at 3.0 mA cm^{-2} with a capacity of 1 mAh cm^{-2}. (e) Nyquist plots of Li||MCNCF after 1, 50, and 100 cycles at 1 mA cm^{-2}. (f) Constant current of symmetric CF@Li, CCF@Li and MCNCF@Li cells at 1 mA cm^{-2}. (g) Rate performance of the symmetric CF@Li, CCF@Li and MCNCF@Li cells with a cycled capacity of 1 mAh cm^{-2}. (h) Comparison of the overpotential at different current densities. (i) Tafel plots for symmetric CF@Li, CCF@Li and MCNCF@Li cells. (j) Radar plot comparing the performance of MCNCF electrode with recent studies reported in the literature.[29–36].

deposition/dissolution dynamics.[25,26] Further corroboration of the superior reaction kinetics is provided by Tafel plot analyses and exchange current density (ECD) measurements (Fig. 4**i**). Among these, the ECD for the MCNCF@Li electrode is determined to be 3.64 mA cm^{-2}, significantly exceeding the 1.64 mA cm^{-2} for CCF@Li and the 0.6 mA cm^{-2} for CF@Li, indicative of a faster charge transfer and reaction kinetics of MCNCF@Li.[27,28] With regards to the most recently reported 3D Li hosts under analogous experimental conditions, to the best of our knowledge, MCNCF exhibits unparalleled electrochemical performance characterized by a very low overpotential and very long cycle life (Fig. 4**j**).

2.5. Ex situ morphology examinations of MCNCF

Ex situ SEM images were taken to evaluate the electrode morphology as well as the formation of Li dendrites and electrochemically inactive, i.e., "dead" Li. After 50 cycles at a current density of 2 mA cm^{-2}, the symmetric cells were dismantled, and the electrodes were examined using SEM at multiple magnifications. The recovered CF@Li electrode exhibits a coarse morphology with visible fissures. In addition, a conspicuous clustering of "dead" Li on the uppermost layer is observed (Fig. S20a**, d**). A similar observation is made for the recovered CCF@Li electrode, from which a significant coalescence of "dead" Li on the surface indicates a nonuniform Li plating/stripping process (Fig. S20b**, e**). The cross-sectional SEM images also reveal an extensive formation of "dead" Li within the CF@Li and CCF@Li structures (Fig. S21a**, b**). In contrast, the recovered MCNCF@Li electrode displays a rather smooth and dense surface (Fig. S20c**, f**). The cross-sectional SEM analysis highlights the reduced formation of "dead" Li with the outer scaffold remaining discernible and the major Li predominantly located in the bottom layer (Fig. S21c). This confirms the effective inhibition of Li dendrite proliferation exerted by the lithiophilicity gradient design, which contributes to the superior cycling stability of the MCNCF electrodes. Moreover, the cycled MCNCF@Li electrode surface exhibits a negligible presence of "dead" Li.

The structural integrity of the cycled 3D MCNCF host was studied through SEM and EDS mapping of the MoN layer. The surface of the cycled MCNCF host maintains a distinct nanowire morphology, indicating the preservation of the nanowire architecture. These nanowires present a thicker and more polished appearance relative to their initial state, which is attributable to the formation of a Li_3N-enriched SEI (Fig. 5**a-d**). EDS mapping further evidences the homogenous dispersion of Cu, Mo, and N, with no observable discontinuities, thereby corroborating the structural resilience of the nanowires over cycling (Fig. 5**e**). Based on the EDS mapping, the presence of elements such as F and S is presumably coming from the decomposed lithium salt, a further validation of the formation of a relatively stable and uniform SEI layer. Fig. 5**f, g** provide schematic representations to elucidate the structural evolution. Without the MoN layer, the CF/CCF substrates trigger the initial Li "top-deposition" behavior and further develop into nonuniform dendritic Li upon repeated Li plating/stripping. The extended dendritic growth, coupled with the continuous reaction with the electrolyte, results in the loss of active Li, which is detrimental to the long-term cycling performance of the CF@Li and CCF@Li electrodes. On the contrary, MCNCF@Li enables a beneficial "bottom-up" Li deposition initially, and allows for a firm adherence of Li to its scaffold before cycling, followed by a surface smoothening effect upon cycling.

2.6. Evaluation of the MCNCF electrodes in full-cells

For assessing the practical use of MCNCF@Li in full-cells, the electrodes were coupled with $LiFePO_4$ (LFP) cathodes. Cyclic voltammetry (CV) reveals distinct reduction and oxidation peaks (R1 and O1) for the MCNCF@Li||LFP cell configuration across the varying sweep rates applied (0.1–1.0 mV s^{-1}). Compared to those of the CF@Li||LFP and CCF@Li||LFP cells, the MCNCF@Li||LFP cell presents a smaller voltage separation between R1 and O1 and higher peak currents (Fig. 6**a and** Fig. S22), indicating a faster and more reversible Li^+ insertion/extraction. Fig. 6**b** provides evidence supporting the assertion that the peak currents in these cells follow a linear relationship with the square root of the sweep rate, highlighting the dominant role of Li^+ diffusion in the electrochemical processes of the cell.[37]

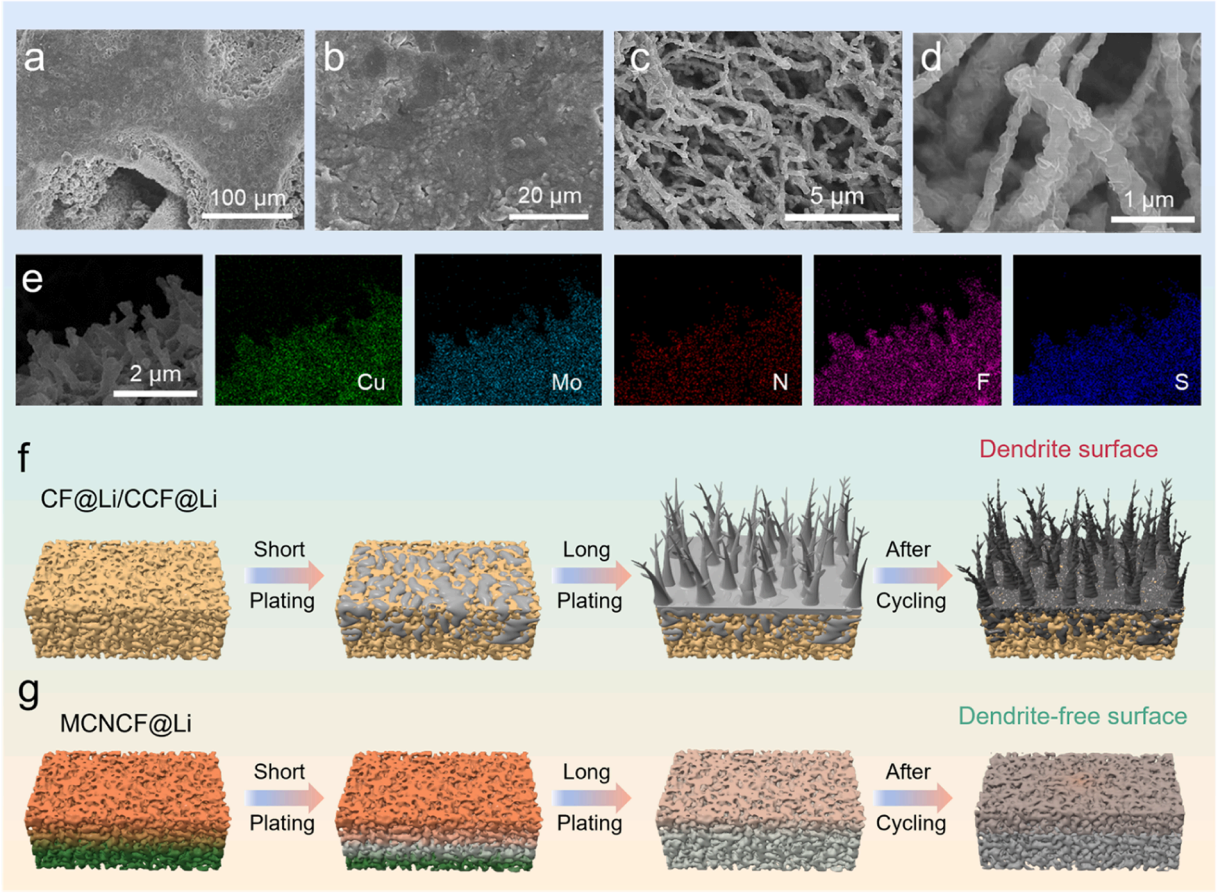

Fig. 5. (a-d) SEM and (e) EDS mapping of the bottom of a recovered MCNCF@Li electrode after cycling. Schematic illustration of the structural evolution of (f) CF@Li and CCF@Li as well as (g) MCNCF@Li electrodes.

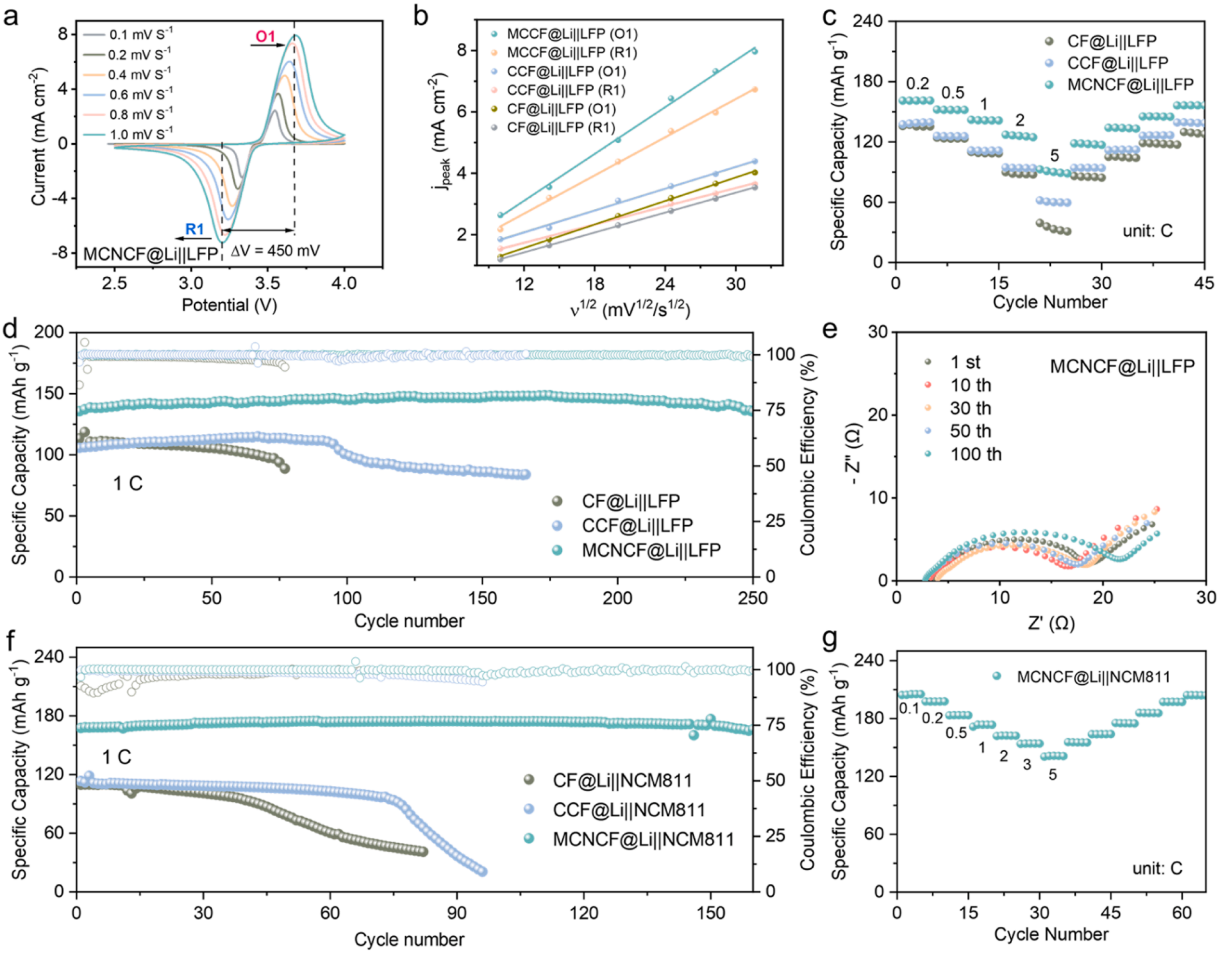

Fig. 6. (a) Typical CV curves of a MCNCF@Li||LFP full-cell at different scan rates (0.1–1.0 mV s^{-1}) and (b) the corresponding linear fit of the reduction/oxidation peak current intensities as a function of the square root of the scan rates. (c) Rate performance and (d) long-term cycling of LFP-based full-cells with different anodes. (e) Nyquist plots of a MCNCF@Li||LFP full-cell at different cycles. (f) Cycling performance of NCM811-based cells with different anodes. (g) Rate performance of an MCNCF@Li||NCM811 cell.

The rate performance of the MCNCF@Li||LFP (N/P ratio of ~7), CCF@Li||LFP and CF@Li||LFP cells is illustrated in Fig. 6**c**. Evidently, with dis-/charge rates from 0.2 C to 5 C, the delivered specific capacities of the MCNCF@Li||LFP cell are 161, 152, 141, 125, and 91 mAh g^{-1} at 0.2 C, 0.5 C, 1 C, 2 C, and 5 C, respectively, pronouncedly surpassing the capacities recorded for the CCF@Li||LFP (139, 126, 111, 94, and 60 mAh g^{-1}) and CF@Li||LFP full-cells (136, 126, 111, 88, and 32 mAh g^{-1}). Subsequently, fresh full-cells were prepared to evaluate their long-term cycling performance at a dis-/charge rate of 1 C. The initial specific capacity for the MCNCF@Li||LFP cell is 137 mAh g^{-1}, outperforming the CCF@Li||LFP and CF@Li||LFP cells, which delivered only 106 mAh g^{-1} and 113 mAh g^{-1}, respectively (Fig. 6**d**). Following a constant current dis-/charge test over 250 cycles, the MCNCF@Li||LFP cell maintains an average CE of 99.93 % and exhibits an impressive capacity retention rate of 99 % with a specific capacity of 135 mAh g^{-1}. In contrast, the CCF@Li||LFP and CF@Li||LFP cells could be cycled only for 165 and 75 cycles, respectively, with substantially lower discharge capacities of 84 and 89 mAh g^{-1}. The galvanostatic charge-discharge profiles for the MCNCF@Li||LFP cell show a much lower polarization and excellent capacity retention, especially when compared to the other two cells (Fig. S23). EIS was conducted to probe the interfacial stability and reaction kinetics of the full-cells during cycling. As illustrated in Fig. 6**e**, the impedance of the MCNCF@Li||LFP full-cell remains essentially consistent over 100 cycles with a lower impedance value, whereas the resistance of the CF@Li||LFP and CCF@Li||LFP cells displays a considerably increasing trend (Fig. S24). The lower impedance of the MCNCF@Li||LFP cell can be attributed to (i) the lithiophilicity gradient architecture within the MCNCF, which promotes a more homogenous Li^+ flux and deposition, and (ii) the reinforced interfacial stability originating from the high ionic conductivity and diminished electronic conductivity of the Li_3N-rich SEI. Consequently, the MCNCF@Li enables a significantly extended cycle life of LFP-based full-cells.

To further demonstrate the potential of MCNCF for practical applications, MCNCF@Li||NCM811 cells (N/P ratio of ~6) were assembled, yielding an impressive initial specific capacity of 167 mAh g^{-1} at 1 C. Notably, an exceptional capacity retention of ca. 99 % is achieved after 160 cycles. In contrast, the retention ratios of the CCF@Li||NCM811 and CF@Li||NCM811 cells sharply drop to 39.96 % and 42.25 %, respectively, after 90 cycles and 80 cycles (Fig. 6**f**). Subsequently, *ex situ* SEM analysis was performed to monitor the surface morphology of the Li anode. After 50 cycles, conspicuous dendrite growth was observed at top of the CF@Li, likely contributing to its deteriorated cycling performance (Fig. S25a**, d**). The *ex situ* SEM image of CCF@Li reveals the formation of a significant amount of "dead Li" on its top surface (Fig. S25b**, e**). In contrast, the surface of cycled MCNCF@Li remains smooth without noticeable dendrite formation (Fig. S25c**, f**). Further, the rate capability of MCNCF@Li is assessed by incrementally increasing the dis-/charge rate from 0.1 C to 5 C (Fig. 6**g**). The specific capacities recorded in sequence are 204, 198, 183, 174, 162, 154, and 141 mAh g^{-1} at 0.1 C, 0.2 C, 0.5 C, 1 C, 2 C, 3 C, and 5 C, respectively. These results indicate that the synergistically engineered lithiophilicity gradient and Li_3N-rich SEI of the MCNCF plays a crucial role in promoting uniform deposition

and dissolution of Li, in turn, enhances the longevity and performance of LMBs.

3. Conclusions

In summary, a combination of ALD and plasma treatment was adopted to fabricate a 3D integrated lithiophilicity gradient structure (MCNCF), successfully guiding the "bottom-up" Li deposition and suppressing dendritic Li growth. The introduction of nanowire structures on the CF skeleton reduces the anode current density and alleviates the volume changes upon cycling. The MoN layer at the bottom of MCNCF preferentially induces uniform Li nucleation. The as-formed Li_3N-enriched SEI layer promotes rapid diffusion of Li^+, enabling a dense and uniform Li deposition. Consequently, the distinctive architecture of the MCNCF host not only exhibits a strong affinity for Li with a very low nucleation overpotential and sustains an exceptional average CE of 97.6 % upon 350 cycles at 0.5 mA cm^{-2} and 1 mAh cm^{-2}. Moreover, the host structure supports a prolonged operational lifespan exceeding 1200 h with efficient mass transfer kinetics at 1 mA cm^{-2} and 1 mAh cm^{-2}. When paired with LFP and NCM811 cathodes, the MCNCF host showcases excellent rate performance and superior cycling stability, making it a viable option for practical applications.

4. Experimental section

Experimental details can be found in the Supporting Information.

CRediT authorship contribution statement

Stefano Passerini: Writing – review & editing, Supervision, Resources, Funding acquisition, Conceptualization. **Minghua Chen:** Writing – review & editing, Supervision, Project administration. **Xin Liu:** Writing – review & editing, Methodology, Data curation. **Dominic Bresser:** Writing – review & editing, Supervision, Funding acquisition. **Yuxuan Wang:** Writing – review & editing, Methodology. **Jian Wang:** Writing – review & editing, Methodology. **Xilai Xue:** Writing – review & editing, Investigation. **Zhen Chen:** Writing – review & editing, Project administration. **Xi Wang:** Writing – review & editing, Writing – original draft, Investigation.

Declaration of Competing Interest

The authors declare that they have no known competing financial interests or personal relationships that could have appeared to influence the work reported in this paper.

Acknowledgements

This work is supported by the National Natural Science Foundation of China (Grant No. 52277215, Grant No. 52377206 and Grant No. 52307237), and the Postdoctoral Science Foundation of China (No. 2023M730884). The authors would like to acknowledge the financial support from the Helmholtz Association and the German Federal Ministry of Education and Research (BMBF) within the ALANO project (03XP0396K).

Appendix A. Supporting information

Supplementary data associated with this article can be found in the online version at doi:10.1016/j.nanoen.2024.110439.

Data Availability

Data will be made available on request.

References

[1] S. Yuan, T. Kong, Y. Zhang, P. Dong, Y. Zhang, X. Dong, Y. Wang, Y. Xia, Advanced electrolyte design for high-energy-density Li-metal batteries under practical conditions. Angew. Chem. 133 (2021) 25828–25842.
[2] X. Zhang, R. Lv, A. Wang, W. Guo, X. Liu, J. Luo, MXene aerogel scaffolds for high-rate lithium metal anodes. Angew. Chem. Int. Ed. 57 (2018) 15028–15033.
[3] Q. Wang, C. Yang, J. Yang, K. Wu, C. Hu, J. Lu, W. Liu, X. Sun, J. Qiu, H. Zhou, Dendrite-free lithium deposition via a superfilling mechanism for high-performance Li-metal batteries. Adv. Mater. 31 (2019) 1903248.
[4] M. Hu, Q. Ma, Y. Yuan, Y. Pan, M. Chen, Y. Zhang, D. Long, Grafting polyethyleneimine on electrospun nanofiber separator to stabilize lithium metal anode for lithium sulfur batteries, Chem. Eng. J. 388 (2020) 124258.
[5] X. Wu, G. He, Y. Ding, Dealloyed nanoporous materials for rechargeable lithium batteries, Electrochem. Energy Rev. 3 (2020) 541–580.
[6] Z. Luo, X. Qiu, C. Liu, S. Li, C. Wang, G. Zou, H. Hou, X. Ji, Interfacial challenges towards stable Li metal anode, Nano Energy 79 (2021) 105507.
[7] X. Zhang, A. Wang, X. Liu, J. Luo, Dendrites in lithium metal anodes: suppression, regulation, and elimination, Acc. Chem. Res. 52 (2019) 3223–3232.
[8] D. Wang, W. Zhang, W. Zheng, X. Cui, T. Rojo, Q. Zhang, Towards High-Safe Lithium Metal Anodes: Suppressing Lithium Dendrites via Tuning Surface Energy, Adv. Sci. 4 (2017) 1600168.
[9] G. Yang, J. Chen, P. Xiao, P.O. Agboola, I. Shakir, Y. Xu, Graphene anchored on Cu foam as a lithiophilic 3D current collector for a stable and dendrite-free lithium metal anode, J. Mater. Chem. A 6 (2018) 9899–9905.
[10] M. Chen, X. Zhou, X. Liang, S. Qiu, Y. Li, Z. Chen, Constructing porous nickel-zinc alloy layer on nickel foam for dendritic-free lithium metal anode, Electrochim. Acta 460 (2023) 142615.
[11] Y. Liu, D. Lin, Z. Liang, J. Zhao, K. Yan, Y. Cui, Lithium-coated polymeric matrix as a minimum volume-change and dendrite-free lithium metal anode, Nat. Commun. 7 (2016) 10992.
[12] B. Yu, T. Tao, S. Mateti, S. Lu, Y. Chen, Nanoflake arrays of lithiophilic metal oxides for the ultra-stable anodes of lithium-metal batteries. Adv. Funct. Mater. 28 (2018) 1803023.
[13] A. Huang, Y. Wu, H. Huang, C. Li, Y. Sun, L. Li, S. Peng, Lithiophilic Mo_2C clusters-embedded carbon nanofibers for high energy density lithium metal batteries, Adv. Funct. Mater. 33 (2023) 2303111.
[14] C. Yang, Y. Yao, S. He, H. Xie, E. Hitz, L. Hu, Ultrafine silver nanoparticles for seeded lithium deposition toward stable lithium metal anode, Adv. Mater. 29 (2017) 1702714.
[15] Y. Huang, B. Chen, J. Duan, F. Yang, T. Wang, Z. Wang, W. Yang, C. Hu, W. Luo, Y. Huang, Graphitic carbon nitride (g-C_3N_4): an interface enabler for solid-state lithium metal batteries, Angew. Chem. Int. Ed. 59 (2020) 3699–3704.
[16] P. Zhai, T. Wang, H. Jiang, J. Wan, Y. Wei, L. Wang, W. Liu, Q. Chen, W. Yang, Y. Cui, Y. Gong, 3D artificial solid-electrolyte interphase for lithium metal anodes enabled by insulator-metal-insulator layered heterostructures, Adv. Mater. 33 (2021) 2006247.
[17] D. Tang, L. Yuan, Y. Liao, W. Jin, J. Chen, Z. Cheng, X. Li, B. He, Z. Li, Y. Huang, Improving the cycling stability of lithium metal anodes using Cu_3N-modified Cu foil as a current collector, Sci. China Mater. 65 (2022) 2385–2392.
[18] W. Cao, W. Chen, M. Lu, C. Zhang, D. Tian, L. Wang, F. Yu, In situ generation of Li_3N concentration gradient in 3D carbon-based lithium anodes towards highly-stable lithium metal batteries, J. Energy Chem. 76 (2023) 648–656.
[19] X. Wang, Z. Chen, K. Jiang, M. Chen, S. Passerini, 3D host design strategies guiding "bottom-up" lithium deposition: a review, Adv. Energy Mater. 14 (2024) 2304229.
[20] X. Shi, A. Wu, H. Yan, L. Zhang, C. Tian, L. Wang, H. Fu, A. MOFs, plus MOFs" strategy toward Co–Mo_2N, Tubes Effic. Electro Overall Water Split. J. Mater. Chem. A 6 (2018) 20100–20109.
[21] K. Inumaru, K. Baba, S. Yamanaka, Structural distortion and suppression of superconductivity in stoichiometric B1-MoN epitaxial thin films, Phys. Rev. B 73 (2006) 052504.
[22] Z. Li, X. Li, L. Zhou, Z. Xiao, S. Zhou, X. Zhang, L. Li, L. Zhi, A synergistic strategy for stable lithium metal anodes using 3D fluorine-doped graphene shuttle-implanted porous carbon networks, Nano Energy 49 (2018) 179–185.
[23] X. Zhang, Y. Chen, K. Srinivas, B. Yu, F. Ma, B. Wang, X. Wang, J. He, Z.L. Xu, Lithiophilic Mo_3N_2/MoN as multifunctional interlayer for dendrite-free and ultra-stable lithium metal batteries, J. Colloid Interface Sci. 612 (2022) 332–341.
[24] H. Ye, S. Xin, Y.X. Yin, J.Y. Li, Y.G. Guo, L.J. Wan, Stable Li plating/stripping electrochemistry realized by a hybrid Li reservoir in spherical carbon granules with 3d conducting skeletons, J. Am. Chem. Soc. 139 (2017) 5916–5922.
[25] Y. Zhao, L. Wang, J. Zou, Q. Ran, L. Li, P. Chen, H. Yu, J. Gao, X. Niu, Bottom-up lithium growth guided by Ag concentration gradient in 3D PVDF framework towards stable lithium metal anode, J. Energy Chem. 65 (2022) 666–673.
[26] Y. Nan, S. Li, Y. Shi, S. Yang, B. Li, Gradient-distributed nucleation seeds on conductive host for a dendrite-free and high-rate lithium metal anode. Small 15 (2019) 1903520.
[27] Y. Fan, J. Liao, D. Luo, Y. Huang, F. Sun, J. Nan, In situ formation of a lithiophilic surface on 3D current collectors to regulate lithium nucleation and growth for dendrite-free lithium metal anodes, Chem. Eng. J. 453 (2023) 139903.
[28] P. Xu, X. Hu, X. Liu, X. Lin, X. Fan, X. Cui, C. Sun, Q. Wu, X. Lian, R. Yuan, A lithium-metal anode with ultra-high areal capacity (50 mAh cm^{-2}) by gridding lithium plating/stripping, Energy Storage Mater. 38 (2021) 190–199.
[29] S. Elumalai, P.L. Joseph, R.R. Mathiarasu, K. Raman, R. Subashchandrabose, Three-Dimensional Octahedral Nanocrystals of Cu_2O/CuF_2 Grown on Porous Cu Foam Act as a Lithophilic Skeleton for Dendrite-Free Lithium Metal Anode, ACS Appl. Mater. Interfaces 15 (2023) 42648–42658.

[30] B. Sun, Q. Zhang, W. Xu, R. Zhao, H. Zhu, W. Lv, X. Li, N. Yang, A gradient topology host for a dendrite-free lithium metal anode, Nano Energy 94 (2022) 106937.
[31] Z. Chen, W. Chen, H. Wang, C. Zhang, X. Qi, L. Qie, F. Wu, L. Wang, F. Yu, Lithiophilic anchor points enabling endogenous symbiotic Li_3N interface for homogeneous and stable lithium electrodeposition, Nano Energy 93 (2022) 106836.
[32] W. Li, S. Zheng, Y. Gao, D. Feng, Y. Ru, T. Zuo, B. Chen, Z. Zhang, Z. Gao, H. Geng, High rate and low-temperature stable lithium metal batteries enabled by lithiophilic 3D Cu-CuSn porous framework, Nano Lett. 23 (2023) 7805–7814.
[33] X. Zhang, J. Chen, P. Li, C. Ayranci, G. Li, High mass loading of edge-exposed Cu_3P nanocrystal in 3D freestanding matrix regulating lithiophilic sites for high-performance lithium metal anode, ACS Appl. Mater. Interfaces 15 (2023) 29352–29362.
[34] G. Peng, Q. Zheng, G. Luo, D. Zheng, S.P. Feng, U. Khan, A.R. Akbar, H. Luo, F. Liu, A gradient lithiophilic structure for stable lithium metal anodes with ultrahigh rate and ultradeep capacity, Small 19 (2023) 2303787.
[35] C. Lu, M. Tian, C. Wei, J. Zhou, M.H. Rümmeli, R. Yang, N. Synergized, P dual-doped 3D carbon host derived from filter paper for durable lithium metal anodes, J. Colloid Interface Sci. 632 (2023) 1–10.
[36] X. Fei, H. Gao, Y. Xu, W. Ma, B. Yu, F. Tan, G. Cheng, Z. Zhang, Porous lithiophilic Cu-Sn solid solution current collector for dendrite-free lithium metal batteries, Energy Storage Mater. 65 (2024) 103079.
[37] J. Wu, Z. Ju, X. Zhang, K.J. Takeuchi, A.C. Marschilok, E.S. Takeuchi, G. Yu, Building efficient ion pathway in highly densified thick electrodes with high gravimetric and volumetric energy densities, Nano Lett. 21 (2021) 9339–9346.

Xi Wang is currently Ph.D. student under the supervision of Prof. Minghua Chen and Prof. Zhen Chen at Harbin University of Science and Technology. Her research interest focuses on lithium metal anodes, especially 3D current collectors, to enable high energy density lithium-metal batteries.

Zhen Chen is currently professor at Harbin University of Science and Technology. She received her B.S. degree at Southeast University (SEU) in China in 2014, and Ph.D. degree at Nanyang Technological University (NTU) in Singapore in 2018. From 2019–2022, she worked as a scientist at Helmholtz Institute Ulm (HIU) of Karlsruhe Institute of Technology (KIT) in Germany. Her research activities mainly focus on the development of key materials and relevant applications in the field of electrochemical energy storage with a special focus on developing high-performance lithium metal secondary batteries.

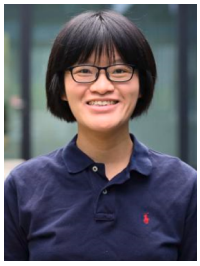

Xilai Xue is currently postdoctoral researcher at the Helmholtz Institute Ulm (HIU) of Karlsruhe Institute of Technology (KIT). She received her PhD from KIT in 2023, MEng from University of Chinese Academy of Sciences in 2020, and BEng from Xiamen University in 2017. Her research mainly focuses on the development of anode materials for Li-ion and Na-ion batteries.

Jian Wang is a research fellow supported by Alexander von Humboldt Foundation in Helmholtz Institute Ulm (HIU) of Karlsruhe Institute of Technology (KIT). He received his Ph.D. degree from University of Science and Technology of China (USTC). His research interests focus on the constructions of catalysis in secondary batteries ("Catalysis-in-Batteries") and the exploration of in-situ/operando characterizations for probing catalytic mechanisms.

Yuxuan Wang is undergraduate student at Harbin University of Science and Technology, studying under the supervision of Prof. Xin Liu. His research interests are mainly electrochemical simulation, especially interface simulation.

Dominic Bresser is currently serving as professor at University Ulm and principal investigator and group leader at the Helmholtz Institute Ulm (HIU) of Karlsruhe Institute of Technology (KIT), Germany. The focus of the group's activities is on the development of advanced lithium and sodium batteries, including new and optimized inorganic and organic electrode materials, sustainable electrode processing technologies, liquid and solid electrolyte systems as well as redox-active polymers.

Xin Liu is Professor at School of Electrical and Electronic Engineering, Harbin University of Science and Technology, China. He earned his B.E. and M.E. degrees from Harbin Institute of Technology, and his Ph.D. from University of Adelaide, Australia. His research focuses on atomic-scale simulations of electrochemical energy storage and conversion systems, particularly aqueous and solid-state batteries, and green hydrogen production. He has co-authored over 40 peer-reviewed articles with over 5500 citations and h-index of 27.

Minghua Chen is currently professor at Harbin University of Science and Technology since 2017. He received Ph.D. from Harbin University of Science and Technology, followed by exchange student and visiting scientist at Nanyang Technological University (NTU) from 2013 to 2016. His research interests are dielectric insulation characteristics of engineering dielectric, and the application and development of new energy materials and devices.

Stefano Passerini is currently senior expert advisor at Austrian Institute of Technology in Vienna (AT). Formerly a professor at Karlsruhe Institute of Technology and University of Muenster (Germany), he co-directed Helmholtz Institute Ulm and MEET Research Center (Germany). His research focuses on the basic understanding and development of materials for high-energy batteries and supercapacitors, with the goal to create sustainable energy storage systems from environmentally friendly and available materials and processes. He is an internationally recognized pioneer in the field of ionic liquids and the development of alkali-ion batteries.